Solar Energy
And Sustainable Development
Refereed, biannual scientific journal issued by:
The Libyan Center for Solar Energy Research and Studies

Comprehensive Analysis of Optoelectronic Properties and Photovoltaic Performance of Rb2CuAsZ6 (Z = Br and Cl) Double Perovskites Using DFT and SCAPS-1D Modelling.

Kamal Assiouan[1*], Hanan Ziani[2], Jamal EL Khamkhami[3], Abdelfattah Achahbar[4].

[1,2,3,4]1Artificial Intelligence and Computational Physics Laboratory, Faculty of Sciences, Abdelmalek Essaadi University, B. P. 2121 M'Hannech II, Tetouan, 93030, Morocco..

E-*mail:* [1]kamal.assiouan@etu.uae.ac.ma , [2]hanane.ziani@etu.uae.ac.ma , [3]jelkhamkhami@uae.ac.ma , [4]aachahbar@uae.ac.ma .

SPECIAL ISSUE ON:

The 1St International Conference on Sciences and Techniques for Renewable Energy and the Environment.
(STR2E 2025)
May 6-8, 2025 at FST-Al Hoceima-Morocco.

KEYWORDS

Density Functional Theory (DFT); Double Perovskites; Rb_2CuAsZ_6 (Z = Br, Cl); Optoelectronic properties; solar cells.

ABSTRACT

Rb_2CuAsZ_6 (Z = Br, Cl) double perovskites were studied for their optoelectronic and photovoltaic properties using a comprehensive density functional theory (DFT) analysis. Using the HSE06 functional for electronic band structure calculations, $Rb_2CuAsBr_6$ and $Rb_2CuAsCl_6$ exhibit indirect band gaps (Eg) of 0.64 eV and 1.09 eV, respectively. Moreover, the analysis of the optical properties revealed substantial absorption (α) around 105 in both the visible and near-infrared regions, highlighting their suitability for solar cell and optoelectronic applications. Moreover, we utilised the absorber layer $Rb_2CuAsCl_6$ to construct an n-i-p structure perovskite and modelled it Using the SCAPS-1d program, this calculation was performed with a thickness of 400 nm of $Rb_2CuAsCl_6$, yielding remarkable performance: an open-circuit voltage Voc of 0.81 V, a short-circuit current density (J_{sc}) of 38.33 mA/cm², a fill factor (FF) of 68.65%, and a power conversion efficiency (PCE) of 20.63%.

*Corresponding author.

DOI: https://doi.org/10.51646/jsesd.v14iSTR2E.802

تحليل شامل للخصائص البصرية الإلكترونية والأداء الكهروضوئي للبيروفسكايت المزدوج Rb_2CuAsZ_6 (Z = Br, Cl) باستخدام نمذجة DFT و SCAPS-1D

كمال أسوان ،حنان الزياني ، جمال الخمخامي، عبد الفتاح اشهبار.

ملخص: تمت دراسة الخصائص البصرية الإلكترونية والكهروضوئية للبيروفسكايت المزدوج Rb_2CuAsZ_6 (Z = Br, Cl) باستخدام نظرية الكثافة الوظيفية (DFT). كشفت حسابات تركيب النطاق الإلكتروني باستخدام الوظيفة HSE06 عن فجوات نطاق غير مباشرة تبلغ 0.64 إلكترون فولت لـ $Rb_2CuAsBr_6$ و 1.09 إلكترون فولت لـ $Rb_2CuAsCl_6$. أظهرت التحليلات البصرية امتصاصًا قويًا حوالي 105 في كل من مناطق الضوء المرئي والأشعة تحت الحمراء القريبة، مما يبرز ملاءمتها للتطبيقات البصرية الإلكترونية والخلايا الشمسية. تم تصميم ومحاكاة هيكل خلية شمسية بيروفسكايت n-i-p تتضمن $Rb_2CuAsCl_6$ كطبقة ماصة باستخدام برنامج SCAPS-1D، وقد تم إجراء هذه الحسابات بسماكة 400 نانومتر من $Rb_2CuAsCl_6$، مما أسفر عن أداء جيد: جهد دائرة مفتوحة (V_{oc}) يبلغ 0.81 فولت، وكثافة تيار دائرة قصيرة (J_{sc}) تبلغ 38.33 مللي أمبير/سم^2، وعامل تعبئة (FF) يبلغ 68.65 %، وكفاءة تحويل الطاقة (PCE) تبلغ 20.63 %.

الكلمات المفتاحية – كنظرية الكثافة الوظيفية (DFT)؛ البيروفسكايت المزدوج؛ Rb_2CuAsZ_6 (Z = Br, Cl)؛ الخصائص البصرية الإلكترونية؛ الخلايا الشمسية.

1. INTRODUCTION

The growing global energy demand, driven by technological and industrial advancements, has heightened the need for clean energy sources to mitigate environmental concerns associated with fossil fuels. Solar and thermoelectric energy have emerged as sustainable and cost-effective solutions[1,2]. As silicon solar cells near their theoretical efficiency limits, researchers are increasingly exploring alternative materials that exhibit superior photovoltaic properties[3].

Organic perovskites, introduced in 2009[4], have emerged as promising alternatives, demonstrating significant advancements in photovoltaic efficiency reaching 25.5% within a decade driven by their exceptional electronic and optical properties[5,6]. However, issues like environmental toxicity (Pb^{2+}) and stability challenges under moisture and heat prompted the development of lead-free double perovskites (LFDPs)[7].

First-principles calculations have enabled researchers to identify eleven materials with suitable bandgaps for photovoltaic absorption, including $Cs_2CuSbCl_6$ and $Rb_2CuSbCl_6$[8,9]. However, only a limited number of these materials, such as $Cs_2AgBiBr_6$[10], $Cs_2AgBiCl_6$[11], and $(CH_3NH_3)_2AgBiBr_6$ [12], have been successfully synthesized. Furthermore, simulations play a crucial role in understanding the properties and performance metrics of various materials, complementing experimental research [13–15]. Recent studies have investigated the Power Conversion Efficiency (PCE) of lead-free double perovskite (LFDP) solar cells using numerical simulations, such as SCAPS-1D[16]. Utsho et al. investigated the use of $Cs_2CuBiBr_6$ as the absorber layer and Cu-based thiogallate (CBTS) as the hole transport layer (HTL), examining the impact of varying electron transport layers (ETLs) including WS_2, C_{60}, PCBM, and TiO_2 on solar cell performance. The corresponding Power Conversion Efficiencies (PCEs) achieved were 19.70%, 18.69%, 19.52%, and 19.65%, respectively[17]. Additionally, a Cs2TiBr6 based double perovskite solar cell (PSC) was simulated using SCAPS-1D and Density Functional Theory (DFT) calculations, confirming a bandgap of 1.6 eV. The cell employed La-doped $BaSnO_3$ (LBSO) as the ETL and $CuSbS_2$ as the HTL. Optimization of the absorber thickness, defect density, and bandgap resulted in an impressive PCE of 29.13%[18]. Moreover, an analysis of the ITO/ETL/$Cs_2AgBiBr_6$/Cu_2O/Au structure, with $Cs_2AgBiBr_6$ as the absorber layer, Cu_2O as the HTL, and TiO_2 as the ETL, achieved a PCE of 18.83%, highlighting the potential of lead-free double perovskite solar cells[19].

This study aims to explore the potential of the double perovskites Rb_2CuAsZ_6 (Z = Br, Cl) for applications in optoelectronic and photovoltaic devices. The investigation will begin with a structural analysis, followed by an in-depth examination of the electronic properties crucial for optoelectronic functionality. Subsequently, the optical characteristics will be calculated up to 10 eV. Finally, the efficiency of $Rb_2CuAsCl_6$ as the absorber layer in a solar cell will be evaluated using SCAPS-1D software.

2. COMPUTATIONAL FRAMEWORKS

2.1. Computation of Rb_2CuAsZ_6 properties using DFT

The optical, electronic, and structural characteristics of the double perovskites Rb_2CuAsZ_6 (Z = Br, Cl) were investigated using density functional theory (DFT) calculations with the Quantum ESPRESSO package[20]. Broyden–Fletcher–Goldfarb–Shanno (BFGS) method was used to optimise the crystal formations[21,22]. The Perdew-Burke-Ernzerhof (PBE) functional was employed to describe the exchange-correlation interaction within the Generalized Gradient Approximation (GGA) framework[23,24]. The convergence criteria for structural optimization were set to 10^{-6} eV/atom for total energy and 10^{-4} eV/Å for the maximum force. An 8 × 8 × 8 Monkhorst-Pack k-point grid was employed for Brillouin zone sampling during the optimization process, ensuring accurate structural relaxation. The kinetic energy cutoff (Ecut) was set at 70 Ry. The calculations of electronic properties, the GGA-PBE was employed with a denser 12 × 12 × 12 k-point grid. To overcome the band gap underestimation inherent to this approximation, the HSE06 hybrid functional with norm-conserving pseudopotentials (NCPP) was used to estimate the band gap.Additionally, the dielectric function was obtained using PBE with norm-conserving pseudopotentials Within the Random-Phase Approximation (RPA) framework, calculations were performed using the Yambo code [25].

2.2. Simulation methodology

The one-dimensional Solar Cell Capacitance Simulator (SCAPS-1D) is a widely used open-source numerical simulation program for analysing solar cell performance. This study aimed to design a double perovskite solar cell and comprehensively evaluate its performance under the Air Mass 1.5 Global (AM1.5G) spectrum by numerically solving Poisson's equation alongside the electron and hole continuity equations[26], using SCAPS-1D version 3.3.11.
Poisson's equation:

$$-\frac{\partial}{\partial x}\left(-\varepsilon(x)\frac{\partial V}{\partial x}\right)=q\left[p(x)-n(x)+N_D^+(x)-N_A^-(x)+p_t(x)-n_t(x)\right] \qquad (1)$$

Continuity equation for electrons:

$$\frac{\partial n}{\partial x}=\frac{1}{q}\frac{\partial J_n}{\partial x}+G_n-R_n \qquad (2)$$

Continuity equation for holes:

$$\frac{\partial p}{\partial x}=\frac{1}{q}\frac{\partial J_p}{\partial x}+G_p-R_p \qquad (3)$$

The following symbols represent the respective physical quantities: q denotes the electronic charge, ε the dielectric permittivity, V the electric potential, p(x) the free hole concentration, n(x) the free electron concentration, $N_A^-(x)$ the concentration of ionized acceptors, $N_D^+(x)$ the

concentration of ionized donors, nt(x) the electron trap density, and pt(x) the hole trap density. Furthermore, the current densities, generation rates, and recombination rates for electrons and holes are represented by J_n, J_p, G_n, G_p, R_n, and R_p, respectively.

3. RESULTS AND DISCUSSION

3.1. Structural Properties

The lead-free double perovskite Rb_2CuAsZ_6 (Z = Br, Cl) crystallizes in a cubic unit cell within the $Fm\bar{3}m$ space group (no. 225), as illustrated in Figure 1.

The Wyckoff positions occupied by Rb, Cu, As, and Br/Cl atoms in the structure are 8c, 4b, 4a, and 24e, respectively. The structural optimisation determines the equilibrium volume at which the material attains its minimum total energy, corresponding to its most stable configuration, known as the ground state energy.

The calculated equilibrium volumes, total energies, and unit cell parameters for the double perovskite structures $Rb_2CuAsBr_6$ and $Rb_2CuAsCl_6$ are summarized in Table 1.

The increase in the ionic radii of the halogens from Cl to Br accounts for the decrease in the lattice constant as we move from $Rb_2CuAsBr_6$ to $Rb_2CuAsCl_6$. Furthermore, the stability of both compounds was evaluated by calculating the Goldschmidt tolerance factor (t_G) using the following formula[27]:

$$t_G = \frac{r_{Rb} + r_Z}{\sqrt{2}\left(\frac{r_{Cu} + r_{As}}{2} + r_Z\right)} \qquad (4)$$

along with the formation energy (E_f), which was calculated using the following expression[28]:

$$E_f^{Rb_2CuAsZ_6} = \left(E_{Rb_2CuAsZ_6} - \left[2E^{Rb} + E^{Cu} + E^{As} + 6E^{Z}\right]\right)/10 \qquad (5)$$

In this context, ERb_2CuAsZ_6 represents the total energy of Rb_2CuAsZ_6 (Z=Br, Cl). The terms E^{Rb}, E^{Cu}, E^{As}, E^{Z} correspond to the energies of isolated Rb, Cu, As and Z (Br, Cl) atoms, respectively, while r_{Rb}, r_{Cu}, r_{As}, and r_Z represents the atomic radii of the Br and Cl atoms.

The negative formation energies calculated for both perovskites, as presented in Table 1, demonstrate their thermodynamic stability. Additionally, the tolerance factor values, which fall within the required range for a cubic structure ($0.8 < t_G < 1.0$), further substantiate the stability of $Rb_2CuAsBr_6$ and $Rb_2CuAsCl_6$, as detailed in Table 1.

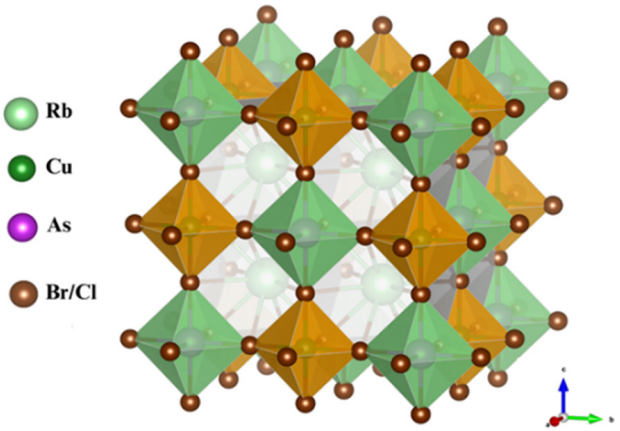

Figure1. FCC (Face-Centered Cubic) crystal structure of Rb_2CuAsZ_6 (Z = Br, Cl).

Table 1 Optimised Cell parameters and phase stability of Rb_2CuAsZ_6 (Z=Br, Cl).

Parameters	$Rb_2CuAsBr_6$	$Rb_2CuAsCl_6$
Lattice Constant (Å)	10.69	10.13
Volume at ground state-V_0 ($a.u^3$)	2072.97	1757.2
Ground State Energy-E_0 (Ry)	-3574.92	-1345.76
Tolerance Factor-t_G	0.98	1
Formation Energy-E_f(eV/atom)	-0.81	-1.17

3.2. Electronic properties

Understanding the electronic properties of a material, such as its energy band gap and density of states, is essential for predicting its performance in photovoltaic and optoelectronic applications. Based on the band structure calculated using the PBE-GGA method, as shown in Figure 2a and Figure 2b, the band gaps are determined to be 0.18 eV (L–X) for $Rb_2CuAsBr_6$ and 0.49 eV (L–X) for $Rb_2CuAsCl_6$, highlighting their semiconducting nature with a small indirect band gap. However, it is well known that the GGA-PBE approximation often underestimates the band gap of double perovskites[29]. Conversely, the use of the HSE06 functional enables the calculation of band gap values that more accurately align with experimental measurements. For $Rb_2CuAsBr_6$ and $Rb_2CuAsCl_6$, the band gaps are determined to be 0.64 eV and 1.09 eV, respectively, as shown in Figure 2c and Figure 2d. the smaller atomic radius of Cl is responsible for the increase in the band gap that results from replacing Br. The bandgap values of these lead-free double perovskites, which $Rb_2CuAsCl_6$ satisfies by falling within the ideal range from 0.9 to 1.6 eV for solar cell efficiency, are a key factor determining their suitability for photovoltaic applications[30].

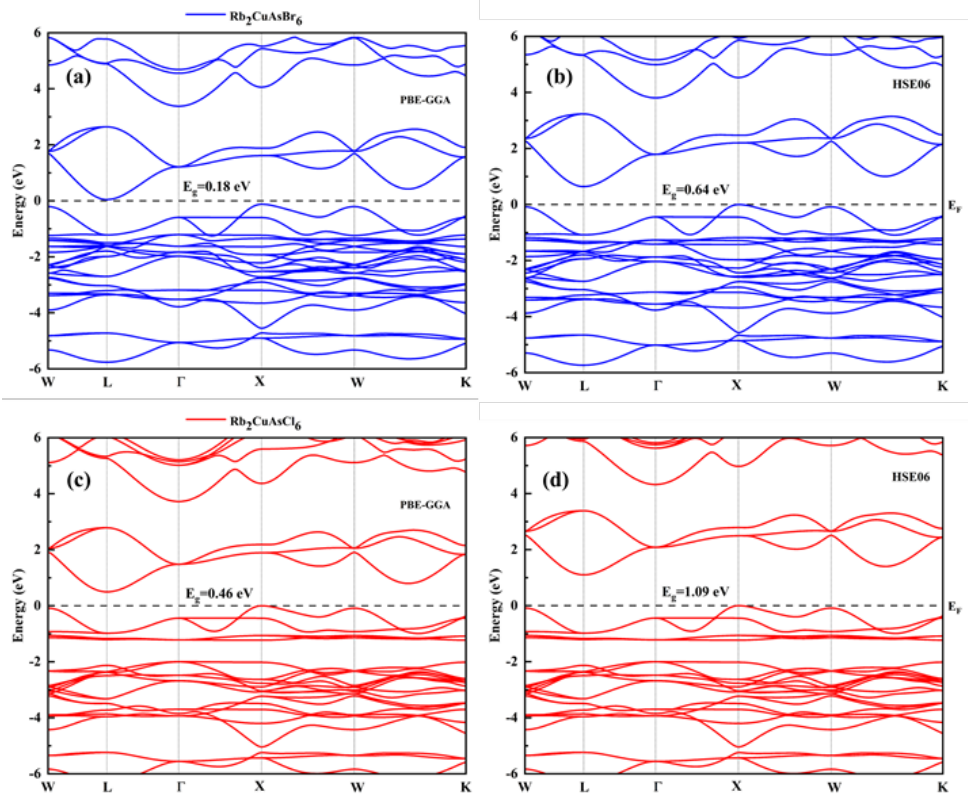

Figure 2. band structures calculated for (a, b) $Rb_2CuAsBr_6$ and (c, d) $Rb_2CuAsCl_6$ using PBE-GGA and HSE06.

A key factor in evaluating the performance of optoelectronic and photovoltaic materials is the effective mass of charge carriers. To assess the performance of these materials in such applications, it is crucial to determine the effective masses of both electrons and holes. Accordingly, using the method described in Equation (6)[31], we fitted a parabolic function near the valence band maximum (VBM) and conduction band minimum (CBM) at high symmetry points (L-X) to calculate the effective masses of electrons and holes.

$$m^* = \hbar^2 \left[\frac{\partial^2 E(k)}{\partial^2 k} \right]^{-1} \qquad (6)$$

Where E(k) represents the energy of the charge carrier as a function of its wave vector, and ħ is the reduced Planck's constant.

The effective masses calculated and presented in Table 2 demonstrate small values for both carrier species, thereby directly enhancing the material's ability to absorb phonons and generate electron pairs. These attributes are critical for the functionality of a variety of applications, including solar cells and optoelectronic devices like LEDs[32].

Table 2. Calculated Effective Mass (m*) and Band Gap (E_g) of Rb_2CuAsZ_6 (X = Br, Cl) Using PBE-GGA and HSE06 Approximations.

Perovskites	PBE (eV)	HSE06 (eV)	$(m_e^*)/m_e$	$(m_h^*)/m_e$	ε(0)
$Rb_2CuAsBr_6$	0.18	0.64	0.26	0.25	9.27
$Rb_2CuAsCl_6$	0.49	1.09	0.36	0.30	6.75

3.3. Optical properties

Calculating optical properties is crucial for advancements in optoelectronic and photovoltaic technology. This analysis is essential for understanding how materials interact with light, particularly their ability to absorb and emit it, which is governed by inter-band and intra-band transitions. In this context, only inter-band transitions are considered due to their significant impact, while intra-band transitions are disregarded due to their lower probabilities and minimal contribution to overall optical properties. This section presents a comprehensive examination of the optical characteristics across the photon energy spectrum from 0 to 10 eV, aiming to evaluate the potential of perovskite materials Rb_2CuAsZ_6 (Z = Br, Cl) for optoelectronic and photovoltaic applications.

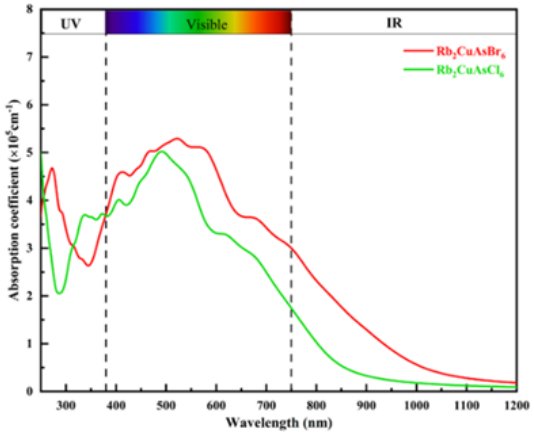

Figure 3. The absorption coefficients as function of wavelength of Rb_2CuAsZ_6 (X=Br, Cl) LFDPs.

Figure 3 displays the absorption coefficient of Rb_2CuAsZ_6 perovskites across a wavelength range from 250 nm to 1200 nm. The absorption edges, occurring around 380 nm for $Rb_2CuAsBr_6$ and 600 nm for $Rb_2CuAsCl_6$, align with their respective band gaps. Notably, $Rb_2CuAsBr_6$ exhibits higher absorption, peaking at 5.31×10^5 cm^{-1} around 525 nm, surpassing $Rb_2CuAsCl_6$, which peaks at 5.02×10^5 cm^{-1} around 490 nm within the visible energy range. Additionally, both perovskite materials also showed significant absorption in the NIR (near-infrared) spectrum. Additionally, the varying band gaps of these materials contribute to their versatility in practical applications. Specifically, $Rb_2CuAsCl_6$ is more suitable for solar cells due to its stability and absorption in the visible spectrum, whereas $Rb_2CuAsBr_6$ is better suited for infrared sensors.

The reflectivity analysis of Rb_2CuAsZ_6 (X=Br, Cl) perovskite, as depicted in Figure 4, reveals static reflection coefficients, with R (0) values of 12% and 17% respectively. Across a wavelength range of 250 nm to 1200 nm, the peak reflectivity remains approximately 40% within the visible spectrum. However, it starts at under 20% in the ultraviolet range, suggesting
that most photons either penetrate the material are absorbed by it.

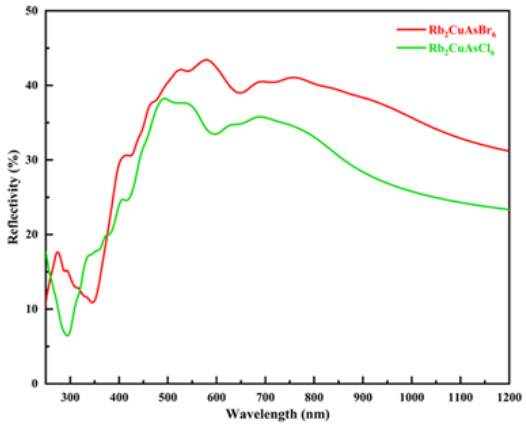

Figure 4. The calculated reflectivity as function of wavelength of Rb_2CuAsZ_6 (X=Br, Cl) LFDPs.

3.4. Efficiency of Perovskite Solar Cells Based on $Rb_2CuAsCl_6$ Absorber Layer

The simulation of photovoltaic (PV) systems, particularly through tools like SCAPS, is an excellent method for assessing the materials' effectiveness in solar cell applications. SCAPS is commonly used in research on thin-film solar cells. It allows researchers to model the thickness of multilayer systems and analyse how various design elements and material parameters influence the photovoltaic efficiency of these devices.

Figure 5 illustrates the perovskite solar cell (PSC) utilises an n-i-p architecture in the device modelling.

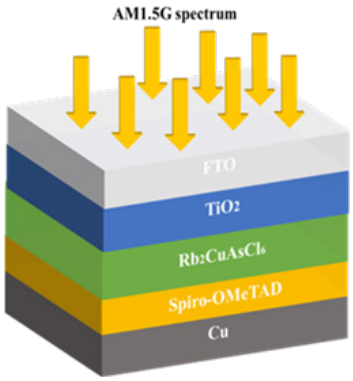

Figure 5. Schematic of the solar cell structure FTO/TiO_2/$Rb_2CuAsCl_6$/Spiro-OMeTAD/Cu.

A Spiro-OMeTAD (hole transport layer-HTL) combined with a titanium dioxide (TiO_2) electron transport layer-(ETL) is separated by the $Rb_2CuAsCl_6$ p-type absorber layer. Fluorine-doped tin oxide (FTO) serves as the front contact anode, while the cathode is composed of copper, which has a work function of 4.65 eV.

Table 3 presents the input parameters used in SCAPS-1D for each layer of the structure, including FTO, TiO_2, $Rb_2CuAsCl_6$, and Spiro-OMeTAD. The listed parameters include the effective density of states in the conduction and valence bands (N^c and Nv), defect density (N_t), band gap energy (E_g), electron affinity (χ), relative permittivity (ε_r), donor and shallow acceptor concentrations (N^d and N_a), electron and hole mobilities (μ_n and μ_p), and layer thicknesses. Furthermore, a uniform thermal velocity of 10^7 cm/s is assumed for both electrons and holes across all layers.

Table 3 The input parameters for SCAPS-1D using the $Rb_2CuAsCl_6$-based solar cell at 300 K.

Parameters	**FTO [33]**	**TiO_2 [34]**	**$Rb_2CuAsCl_6$**	**Spiro-OMeTAD [35]**
Thickness (μm)	0.5	0.1	0.4	0.02
E^g (eV)	3.5	3.2	1.09	2.8
χ (eV)	4.4	4	4.34	2.05
ε_r	9	9	6.75	3
NC ($1/cm^3$)	2×10^{18}	2×10^{18}	5.43×10^{18}	2.2×10^{18}
NV ($1/cm^3$)	1.8×10^{19}	1.8×10^{19}	4.13×10^{18}	1.8×10^{19}
μ_n (cm^2 V/s)	20	100	317	1×10^{-4}
μ_p (cm^2 V/s)	10	25	390	2×10^{-4}
N^D ($1/cm^3$)	10^{15}	10^{16}	10^{15}	0
N^A ($1/cm^3$)	0	0	10^{15}	10^{19}
N^t ($1/cm^3$)	10^{15}	10^{15}	10^{14}	10^{15}

In all our simulations, the temperature was controlled at 300 K, whereas the series (Rs) and shunt resistances (R_{sh}) were fixed at 1 Ω and 103 Ω, respectively, with an illumination intensity of 1000 W/m² under AM1.5G conditions.

Figure 6a displays the energy levels of the layers, whereas Figure 6b illustrates the band diagram of the FTO/TiO_2/$Rb_2CuAsCl_6$/Spiro-OMeTAD/Cu cell.

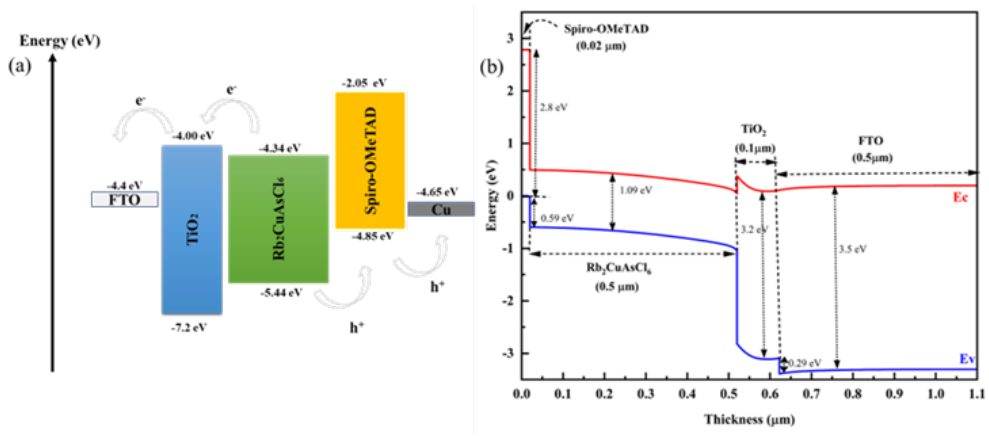

Figure 6. (a) band alignment (b) Diagram of the band energy determined by SCAPS simulation.

At the TiO_2/$Rb_2CuAsCl_6$ interface, the presence of a TiO_2 layer is associated with the formation of a built-in field and a notable VBO (Valence-Band Offset) of 2.9 eV. This configuration effectively impedes the movement of holes towards the TiO_2 layer. Conversely, the CBO (Conduction Band

Offset) of 0.52 eV at the $TiO_2/Rb_2CuAsCl_6$ interface is relatively low, facilitating efficient electron movement from $Rb_2CuAsCl_6$ to TiO_2 and subsequent collection by the FTO (fluorine doped tin oxide) electrode. Moreover, the substantial barrier at the $Rb_2CuAsCl_6$/HTL interface (Spiro-OMeTAD = 0.9 eV) and the intrinsic field at the $Rb_2CuAsCl_6$/hole transport layer interface, this can be ascribed to the organic HTL's higher least-occupied molecular orbital (LUMO) level, which facilitates efficient electron blocking. Holes can easily migrate to the electrode due to the small energy offset at the $Rb_2CuAsCl_6$/Spiro-OMeTAD interface, measured at 0.59 eV.

Figure 7a illustrates the variation in ETL (TiO_2) thickness within the range of 20 to 100 nm and examines its impact on PCE and FF. The results show that at thinner layers, particularly below 30 nm, both PCE and FF are reduced due to the increased prominence of defects. These defects create direct contact points between the perovskite and the cathode, leading to charge recombination. Furthermore, increasing the TiO_2 thickness mitigates recombination by providing more efficient charge transport pathways, thereby improving both PCE and FF. The performance stabilises at a thickness of approximately 100 nm.

Furthermore, the variation of PCE and FF as a function of HTL (Spiro-OMeTAD) thickness, as shown in Figure 7b, demonstrates that both parameters decrease linearly with increasing HTL thickness. This decline can be attributed to the introduction of bulk defects in thicker HTLs, which facilitate non-radiative recombination. Such recombination reduces the number of collected charge carriers, thereby adversely affecting both PCE and FF.

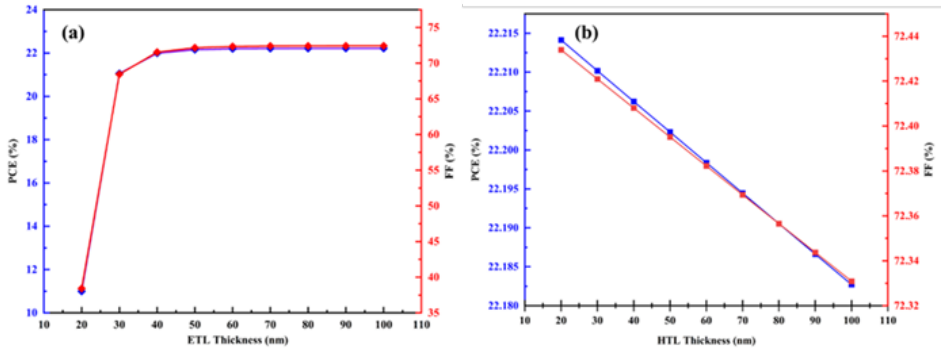

Figure 7. PCE and Fill Factor (FF) versus Thickness for (a) ETL Layer and (b) HTL Layer.

The PCE and FF of the absorber layer are optimized by varying its thickness from 300 nm to 1000 nm, as illustrated in Figure 8.

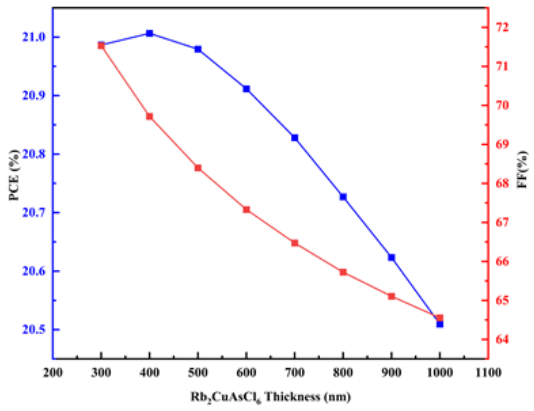

Figure 8. The effect of the absorber layer thickness on PCE and FF.

The PCE increased with thickness, reaching a maximum at 400 nm, with the highest efficiency recorded at 20.63%. However, beyond this optimal thickness, the PCE declined. Nevertheless, the

PCE decreased beyond this optimal thickness, as the perovskite thickness exceeded the carrier diffusion lengths for both electrons and holes, despite the enhanced generation of charge carriers, resulting in higher rates of recombination and, consequently, a decrease in efficiency. Moreover, the FF values fall dramatically with increasing $Rb_2CuAsCl_6$ layer thickness.

Numerous defect types, including vacancies, interstitials, Schottky, and Frenkel defects, can be observed in the perovskite layer. At high defect concentrations (N_t), the stability of perovskite solar cells (PSCs) is significantly reduced. In addition, high defect concentrations also affect carrier mobility by impeding the collection process, further reducing the fill factor and overall efficiency.

The effect of the absorber layer defect density on device performance was examined by modelling the system's efficiency across a range of absorber defect densities, from 10^{13} cm^{-3} to 10^{18} cm^{-3}. The power conversion efficiency (η) for each absorber defect density is shown in Figure 9, along with the J-V characteristics for each defect density. The results indicate a decrease in efficiency from 25.21% to 5.62% over this range.

The open-circuit voltage (V_{oc}) shows a clear decline, attributed to enhanced non-radiative recombination, which raises the saturation current (J_0) according to the formula[36]:

$$V_{oc} = \frac{nK_BT}{q} ln\left(\frac{J_{sc}}{J_0} + 1\right) \qquad (7)$$

where K_B is the Boltzmann constant, q is the elementary charge, J_{sc} is the short-circuit current density, J_0 is the saturation current density and n stands for the ideality factor.

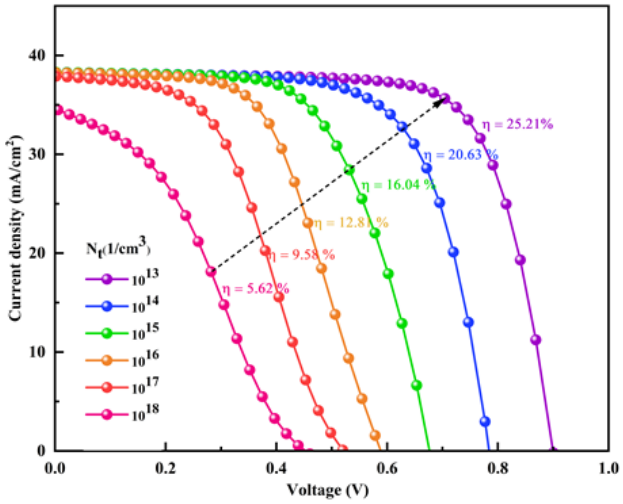

Figure 9. J-V characteristics for varying concentrations of absorber defects.

According to Table 4, $Rb_2CuAsCl_6$ exhibits a notable improvement in efficiency, characterized by higher $V_{oc,}$ J_{sc}, and fill factor (FF), compared to other lead-free double perovskites, such as $Cs_2CuBiBr_6$, Rb_2SnI_6, Cs_2BiAgI_6, and $Cs_2AgBiCl_6$-based solar cells. These further underscores its potential for future solar cell applications. Under an AM 1.5 solar spectrum, the maximum Shockley-Queisser efficiency limit for a single-junction solar cell is approximately 33% for a band gap of 1.4 eV. With a band gap of 1.09 eV, the efficiency of $Rb_2CuAsCl_6$-based solar cells in our study was 20.63%, corresponding to 62% of the theoretical limit.

Despite advancements, several challenges persist, including the occurrence of defects and contaminants during experimental fabrication. These defects serve as recombination centers in solar materials, thereby diminishing the efficiency of solar cells composed of this material.

Consequently, addressing these issues remains a key area of investigation within the scientific community.

Table 4. A comparative analysis of the single-junction solar cell results obtained in this work in relation to experimental and theoretical findings reported in previous research.

Device structure	Photovoltaic parameters				Type of research -Year	References
	V_{oc} (V)	J_{sc} (mA/cm^2)	FF (%)	η (%)		
ITO/Cu-NiO/$Cs_2AgBiBr_6$/C_{60}/BCP/Ag	1.01	3.19	69.2	2.23	Experimental-2018	[37]
ITO/SnO2/$Cs_2AgBiBr_6$/spiro-OMeTAD/Au	0.92	11.40	60.93	6.37	Experimental- 2022	[38]
ITO/ZnO/Cs_2BiAgI_6/CBTS/Au	1.08	23.76	83.78	21.59	Simulation-2022	[39]
ITO/WS_2/Rb_2SnI_6/CdTe/Ni	1.08	44.67	82.71	24.95	Simulation-2024	[40]
ITO/TiO_2/$Cs_2CuBiBr_6$/CBTS/Ni	0.71	35.62	77.52	19.65	Simulation- 2025	[41]
FTO/TiO_2/$Rb_2CuAsCl_6$/spiro-OMeTAD/Au	0.81	38.33	68.65	20.63	Simulation-2025	This work

4. CONCLUSION

The structural and optoelectronic characteristics of the lead-free double perovskites Rb_2CuAsZ_6 (Z = Br, Cl) were thoroughly analysed in this work. Formation energy calculations and the tolerance factor were used to assess structural stability. Using the HSE06 approach, indirect band gaps (Eg) of 0.64 eV and 1.09 eV were found for $Rb_2CuAsBr_6$ and $Rb_2CuAsCl_6$, respectively. Due to their high optical absorption coefficients (approximately 10^5 cm ^{1}), predominantly in the infrared-visible wavelength region, these materials exhibit significant potential as optoelectronic and photovoltaic materials.

Additionally, the use of a planar n-i-p PSC with an absorber layer composed of $Rb_2CuAsCl_6$ was proposed. By adjusting the absorber's defect density and the thicknesses of the hole transport layer (HTL), electron transport layer (ETL), and perovskite absorber layer, SCAPS-1D simulations were used to thoroughly analyse the performance of the PSC. The optimised device demonstrated a fill factor-(FF) of 68.65% and a power conversion efficiency-(PCE) of 20.63%.

Acknowledgment: The authors would like to acknowledge HPC-MARWAN for providing the cloud computing research facility, which is funded by the CNRST (National Centre for Scientific and Technical Research) in Rabat, Morocco. We also extend our appreciation to Professor Marc Burgelman of ghent university, Belgium, for kindly granting us access to the SCAPS-1d program.

REFERENCES

[1] T.D. Lee, A.U. Ebong, A review of thin film solar cell technologies and challenges, Renewable and Sustainable Energy Reviews 70 (2017) 1286–1297. https://doi.org/10.1016/j.rser.2016.12.028.

[2] G.M. Mustafa, A. Slam, S. Saba, N.A. Noor, M. Waqas Iqbal, A. Dahshan, Optoelectronic and thermoelectric characteristics of halide based double perovskites K2YAgX6 (X = Br, I) for energy storage applications, Polyhedron 229 (2023) 116184. https://doi.org/10.1016/j.poly.2022.116184.

[3] A. Augusto, J. Karas, P. Balaji, S.G. Bowden, R.R. King, Exploring the practical efficiency limit

of silicon solar cells using thin solar-grade substrates, J. Mater. Chem. A 8 (2020) 16599–16608. https://doi.org/10.1039/D0TA04575F.

[4] A. Kojima, K. Teshima, Y. Shirai, T. Miyasaka, Organometal Halide Perovskites as Visible-Light Sensitizers for Photovoltaic Cells, J. Am. Chem. Soc. 131 (2009) 6050–6051. https://doi.org/10.1021/ja809598r.

[5] H. Min, D.Y. Lee, J. Kim, G. Kim, K.S. Lee, J. Kim, M.J. Paik, Y.K. Kim, K.S. Kim, M.G. Kim, T.J. Shin, S. Il Seok, Perovskite solar cells with atomically coherent interlayers on SnO2 electrodes, Nature 598 (2021) 444–450. https://doi.org/10.1038/s41586-021-03964-8.

[6] M.A. Green, E.D. Dunlop, M. Yoshita, N. Kopidakis, K. Bothe, G. Siefer, X. Hao, Solar cell efficiency tables (Version 63), Progress in Photovoltaics 32 (2024) 3–13. https://doi.org/10.1002/pip.3750.

[7] B.P. Kore, M. Jamshidi, J.M. Gardner, The impact of moisture on the stability and degradation of perovskites in solar cells, Mater. Adv. 5 (2024) 2200–2217. https://doi.org/10.1039/D3MA00828B.

[8] A. Mera, G. Nazir, Q. Mahmood, N.A. Kattan, T. Alshahrani, A. Rehman, H. Sultana, M.A. Amin, H. Elhosiny Ali, The bandgap engineering of double perovskites Cs2CuSbX6 (X = Cl, Br, I) for solar cell and thermoelectric applications, Inorganic Chemistry Communications 148 (2023) 110303. https://doi.org/10.1016/j.inoche.2022.110303.

[9] Q. Mahmood, G.M. Mustafa, N.A. Kattan, T. Alshahrani, N. Sfina, A. Mera, Z. Hussain Shah, H.H. Somaily, S. Alharthi, M.A. Amin, Tunning of band gap of double perovskites halides Rb2CuSbX6 (X = Cl, Br, I) for solar cells and energy harvesting, Materials Science and Engineering: B 286 (2022) 116088. https://doi.org/10.1016/j.mseb.2022.116088.

[10] A.H. Slavney, T. Hu, A.M. Lindenberg, H.I. Karunadasa, A Bismuth-Halide Double Perovskite with Long Carrier Recombination Lifetime for Photovoltaic Applications, J. Am. Chem. Soc. 138 (2016) 2138–2141. https://doi.org/10.1021/jacs.5b13294.

[11] E.T. McClure, M.R. Ball, W. Windl, P.M. Woodward, Cs2 AgBiX6 (X = Br, Cl): New Visible Light Absorbing, Lead-Free Halide Perovskite Semiconductors, Chem. Mater. 28 (2016) 1348–1354. https://doi.org/10.1021/acs.chemmater.5b04231.

[12] Z. Deng, F. Wei, F. Brivio, Y. Wu, S. Sun, P.D. Bristowe, A.K. Cheetham, Synthesis and Characterization of the Rare-Earth Hybrid Double Perovskites: (CH3 NH3)2 KGdCl6 and (CH3 NH3)2 KYCl6, J. Phys. Chem. Lett. 8 (2017) 5015–5020. https://doi.org/10.1021/acs.jpclett.7b02322.

[13] T. Minemoto, M. Murata, Theoretical analysis on effect of band offsets in perovskite solar cells, Solar Energy Materials and Solar Cells 133 (2015) 8–14. https://doi.org/10.1016/j.solmat.2014.10.036.

[14] F. Liu, J. Zhu, J. Wei, Y. Li, M. Lv, S. Yang, B. Zhang, J. Yao, S. Dai, Numerical simulation: Toward the design of high-efficiency planar perovskite solar cells, Applied Physics Letters 104 (2014) 253508. https://doi.org/10.1063/1.4885367.

[15] H. Sabbah, Numerical Simulation of 30% Efficient Lead-Free Perovskite CsSnGeI3-Based Solar Cells, Materials 15 (2022) 3229. https://doi.org/10.3390/ma15093229.

[16] M. Burgelman, P. Nollet, S. Degrave, Modelling polycrystalline semiconductor solar cells, Thin Solid Films 361–362 (2000) 527–532. https://doi.org/10.1016/S0040-6090(99)00825-1.

[17] K.I. Ferdous Utsho, S.M.G. Mostafa, Md. Tarekuzzaman, M.S.M. Al-Saleem, N.I. Nahid, J.Y. Al-Humaidi, Md. Rasheduzzaman, M.M. Rahman, Md.Z. Hasan, Optimizing Cs2 CuBiBr6 double halide perovskite for solar applications: the role of electron transport layers in SCAPS-1D simulations, RSC Adv. 15 (2025) 2184–2204. https://doi.org/10.1039/D4RA08515A.

[18] K. Shivesh, I. Alam, A.K. Kushwaha, M. Kumar, S.V. Singh, Investigating the theoretical performance of Cs2TiBr6-based perovskite solar cell with La-doped BaSnO3 and CuSbS2 as the charge transport layers, Intl J of Energy Research 46 (2022) 6045–6064. https://doi.org/10.1002/er.7546.

[19] M. Mehrabian, M. Taleb-Abbasi, O. Akhavan, Effects of electron transport layer type on the performance of Pb-free Cs2AgBiBr6 double perovskites: a SCAPS-1D solar simulator–based study, Environ Sci Pollut Res 30 (2023) 118754–118763. https://doi.org/10.1007/s11356-023-30732-0.

[20] P. Giannozzi, S. Baroni, N. Bonini, M. Calandra, R. Car, C. Cavazzoni, D. Ceresoli, G.L. Chiarotti, M. Cococcioni, I. Dabo, A. Dal Corso, S. De Gironcoli, S. Fabris, G. Fratesi, R. Gebauer, U. Gerstmann, C. Gougoussis, A. Kokalj, M. Lazzeri, L. Martin-Samos, N. Marzari, F. Mauri, R. Mazzarello, S. Paolini, A. Pasquarello, L. Paulatto, C. Sbraccia, S. Scandolo, G. Sclauzero, A.P. Seitsonen, A. Smogunov, P. Umari, R.M. Wentzcovitch, QUANTUM ESPRESSO: a modular and open-source software project for quantum simulations of materials, J. Phys.: Condens. Matter 21 (2009) 395502. https://doi.org/10.1088/0953-8984/21/39/395502.

[21] D. Goldfarb, A family of variable-metric methods derived by variational means, Math. Comp. 24 (1970) 23–26. https://doi.org/10.1090/S0025-5718-1970-0258249-6.

[22] D.F. Shanno, Conditioning of quasi-Newton methods for function minimization, Math. Comp. 24 (1970) 647–656. https://doi.org/10.1090/S0025-5718-1970-0274029-X.

[23] J.P. Perdew, K. Burke, M. Ernzerhof, Generalized Gradient Approximation Made Simple, Phys. Rev. Lett. 77 (1996) 3865–3868. https://doi.org/10.1103/PhysRevLett.77.3865.

[24] J.P. Perdew, J.A. Chevary, S.H. Vosko, K.A. Jackson, M.R. Pederson, D.J. Singh, C. Fiolhais, Atoms, molecules, solids, and surfaces: Applications of the generalized gradient approximation for exchange and correlation, Phys. Rev. B 46 (1992) 6671–6687. https://doi.org/10.1103/PhysRevB.46.6671.

[25] A. Marini, C. Hogan, M. Grüning, D. Varsano, yambo: An ab initio tool for excited state calculations, Computer Physics Communications 180 (2009) 1392–1403. https://doi.org/10.1016/j.cpc.2009.02.003.

[26] H. El-assib, M. Alla, S. Tourougui, M. Alla, F. Elfatouaki, S.A. Dar, A. Chauhan, Naima, N. Chawki, N. Shrivastav, V. Manjunath, M. Rouchdi, B. Fares, High-performance optimization and analysis of $Cs_2CuSbCl_6$-Based lead-free double perovskite solar cells with theoretical efficiency exceeding 27 %, Renewable Energy 239 (2025) 122092. https://doi.org/10.1016/j.renene.2024.122092.

[27] V.M. Goldschmidt, Die Gesetze der Krystallochemie, Naturwissenschaften 14 (1926) 477–485. https://doi.org/10.1007/BF01507527.

[28] S.M. Alqahtani, A.Q. Alsayoud, F.H. Alharbi, Structures, band gaps, and formation energies of highly stable phases of inorganic ABX3 halides: A = Li, Na, K, Rb, Cs, Tl; B = Be, Mg, Ca, Ge, Sr, Sn, Pb; and X = F, Cl, Br, I, RSC Adv. 13 (2023) 9026–9032. https://doi.org/10.1039/D3RA00185G.

[29] W. Li, Z. Wang, X. Xiao, Z. Zhang, A. Janotti, S. Rajasekaran, B. Medasani, Predicting band gaps and band-edge positions of oxide perovskites using density functional theory and machine learning, Phys. Rev. B 106 (2022) 155156. https://doi.org/10.1103/PhysRevB.106.155156.

[30] Md.H. Miah, M.U. Khandaker, Md.B. Rahman, M. Nur-E-Alam, M.A. Islam, Band gap tuning of perovskite solar cells for enhancing the efficiency and stability: issues and prospects, RSC Adv. 14 (2024) 15876–15906. https://doi.org/10.1039/D4RA01640H.

[31] S. Zhao, K. Yamamoto, S. Iikubo, S. Hayase, T. Ma, First-principles study of electronic and optical properties of lead-free double perovskites Cs2NaBX6 (B = Sb, Bi; X = Cl, Br, I), Journal of Physics and Chemistry of Solids 117 (2018) 117–121. https://doi.org/10.1016/j.jpcs.2018.02.032.

[32] S. Ghosh, H. Shankar, P. Kar, Recent developments of lead-free halide double perovskites: a new superstar in the optoelectronic field, Mater. Adv. 3 (2022) 3742–3765. https://doi.org/10.1039/D2MA00071G.

[33] V. Deswal, S. Kaushik, R. Kundara, S. Baghel, Numerical simulation of highly efficient Cs2AgInBr6-based double perovskite solar cell using SCAPS 1-D, Materials Science and Engineering: B 299 (2024) 117041. https://doi.org/10.1016/j.mseb.2023.117041.

[34] G. Pindolia, S.M. Shinde, P.K. Jha, Optimization of an inorganic lead free RbGeI3 based perovskite solar cell by SCAPS-1D simulation, Solar Energy 236 (2022) 802–821. https://doi.org/10.1016/j.solener.2022.03.053.

[35] B.K. Ravidas, M.K. Roy, D.P. Samajdar, Investigation of photovoltaic performance of lead-free CsSnI3-based perovskite solar cell with different hole transport layers: First Principle Calculations and SCAPS-1D Analysis, Solar Energy 249 (2023) 163–173. https://doi.org/10.1016/j.solener.2022.11.025.

[36] A. Amjad, S. Qamar, C. Zhao, K. Fatima, M. Sultan, Z. Akhter, Numerical simulation of lead-free vacancy ordered Cs2 PtI6 based perovskite solar cell using SCAPS-1D, RSC Adv. 13 (2023) 23211–23222. https://doi.org/10.1039/D3RA04176J.

[37] W. Gao, C. Ran, J. Xi, B. Jiao, W. Zhang, M. Wu, X. Hou, Z. Wu, High-Quality Cs2 AgBiBr6 Double Perovskite Film for Lead-Free Inverted Planar Heterojunction Solar Cells with 2.2 % Efficiency, ChemPhysChem 19 (2018) 1696–1700. https://doi.org/10.1002/cphc.201800346.

[38] Z. Zhang, Q. Sun, Y. Lu, F. Lu, X. Mu, S.-H. Wei, M. Sui, Hydrogenated Cs2AgBiBr6 for significantly improved efficiency of lead-free inorganic double perovskite solar cell, Nat Commun 13 (2022) 3397. https://doi.org/10.1038/s41467-022-31016-w.

[39] M.K. Hossain, A.A. Arnab, R.C. Das, K.M. Hossain, M.H.K. Rubel, Md.F. Rahman, H. Bencherif, M.E. Emetere, M.K.A. Mohammed, R. Pandey, Combined DFT, SCAPS-1D, and wxAMPS frameworks for design optimization of efficient Cs2 BiAgI6 -based perovskite solar cells with different charge transport layers, RSC Adv. 12 (2022) 34850–34873. https://doi.org/10.1039/D2RA06734J.

[40] M.U. Alam, Md.K.I. Shifat, J.K. Modak, Md. Tarekuzzaman, Md.I. Haque, Md. Rasheduzzaman, M.A. Qader, R. Islam, Y. Arafat, Md.Z. Hasan, Improving the efficiency and performance of Rb2SnI6-based perovskite solar cells through comprehensive optimization: a numerical study, J Comput Electron 24 (2025) 41. https://doi.org/10.1007/s10825-024-02276-0.

[41] K.I. Ferdous Utsho, S.M.G. Mostafa, Md. Tarekuzzaman, M.S.M. Al-Saleem, N.I. Nahid, J.Y. Al-Humaidi, Md. Rasheduzzaman, M.M. Rahman, Md.Z. Hasan, Optimizing Cs2 CuBiBr6 double halide perovskite for solar applications: the role of electron transport layers in SCAPS-1D simulations, RSC Adv. 15 (2025) 2184–2204. https://doi.org/10.1039/D4RA08515A.